Dynamic dissolution and re-adsorption of molybdate ion in iron incorporated nickel-molybdenum oxyhydroxide for promoting oxygen evolution reaction

Hanxiao Liao [a], Xiaodong Zhang [b], Shuwen Niu [c], Pengfei Tan [a,*], Kejun Chen [b], Yong Liu [a], Gongming Wang [c], Min Liu [b,*], Jun Pan [a,*]

[a] *State Key Laboratory for Powder Metallurgy, Central South University, Changsha 410083, China*
[b] *School of Physical and Electronics, Central South University, Changsha 410083, China*
[c] *Department of Chemistry, University of Science and Technology of China, Hefei 230026, China*

A R T I C L E   I N F O

A B S T R A C T

Transition metal-based pre-catalysts undergo drastic reconstruction to form the active catalysts during the alkaline oxygen evolution reaction (OER). However, the effect of escaped inactive ion from pre-catalysts themselves is usually ignored during reconstruction processes. Here, we investigate the effect of inactive MoO_4^{2-} escaped from a pre-catalyst of Fe incorporated nickel-molybdenum oxyhydroxide (NiMo-Fe) on OER performance. The results of *in-situ* Raman and X-ray photoelectron spectroscopy reveal that MoO_4^{2-} can be easily dissolved into KOH electrolyte and re-adsorbed on surface of catalyst during OER processes, which delivers a promoting effect on OER performance. The dissolution of MoO_4^{2-} is beneficial for increasing the reconstruction degree of NiMo-Fe to form the active phase of NiFeOOH. Theoretical calculations demonstrate that the re-adsorbed MoO_4^{2-} is favorable for the adsorption of the OOH* intermediate, thus boosts the OER activity. As expected, the NiMo-Fe shows a superior electrocatalytic performance for OER, outperforming the pre-catalyst without Mo species. This finding enriches the knowledge of inactive-ion effect on alkaline OER performance and offers a path for developing efficient electrocatalysts.

1. Introduction

Developing high-active and low-cost catalysts for oxygen evolution reaction (OER) is indispensable to meet practical requirements of alkaline water electrolysis [1–4]. High-valence transition metal oxyhydroxides catalysts with decently intrinsic activity for alkaline OER are deemed as promising candidates to replace commercial RuO_2 and IrO_2 [5–11]. Most of these catalysts are derived from the pre-catalysts including metal oxides/hydroxides,[12–17] metal alloys [18–20] and metal chalcogenides [21–23] etc., which undergo the drastic structure evolutions during OER processes. Therefore, great efforts focus on the reconstruction of active species from the suitable pre-catalysts under OER conditions. As reported, modifying the pre-catalysts with inactive anions and cations (PO_3^{3-}, BO_3^{3-}, Cr^{3+}, Ba^{2+} and Sr^{2+}) for OER can encourage the reconstruction of pre-catalysts into active phases by the leaching of those ions [24–27]. Among them, molybdate ion (MoO_4^{2-}) have been widely used for this purpose due to its dissolvable property in

the alkaline electrolyte [15,28,29]. Although the leaching of inactive ions induced the reconstruction of pre-catalysts were proposed, the effect of the inactive species generated from pre-catalysts themselves on OER tends to be unnoticed during the electrocatalytic processes. Thus, understanding the inactive-ion effect in those catalysts is imperative for designing efficient catalysts for better OER performances.

Extending knowledge of inactive ions for electrocatalytic reaction is able to construct a highly efficient electrocatalytic environment. Moreover, it has been reported that some special ions in the electrolyte have great influences on the catalytic performance [30–35]. For examples, thiocyanate ions can poison the catalytic sites of most single atomic catalysts to affect their catalytic activities [30,31]. The excessively local concentration of hydrogen ion or potassium ion enables a fast electrocatalytic reaction by improving the absorption or activation of reactant [32–34]. The various alkali metal cations can also adjust the activity and selectivity of metal catalysts by tuning the interaction between reaction intermediates and metal cations [35]. Noticeably, these ions are

introduced by the extra adding into the electrolyte. Thus, the investigations of the overlooked inactive ions derived from pre-catalysts themselves are essential to enrich the knowledge of ion effect in electrochemical energy storage and conversion.

Herein, we disclose the dynamic behavior and the role of inactive MoO_4^{2-} on OER activity under OER conditions. A promising pre-catalyst of amorphous Fe incorporated NiMo oxyhydroxide (denoted as NiMo-Fe) was fabricated via a facile and convenient electrochemical procedure. The dynamic re-adsorption behavior of the dissolved MoO_4^{2-} from NiMo-Fe during OER processes is uncovered by *in-situ* Raman and X-ray photoelectron spectroscopy (XPS). Moreover, a promoting effect of MoO_4^{2-} on OER activity is verified by the experimental data and theoretical calculations. The dissolution of MoO_4^{2-} is able to enhance the reconstruction degree of pre-catalyst to active phase and the surface-adsorbed MoO_4^{2-} can promote the OER activity through facilitating the adsorption of OOH* intermediate of. As a consequence, the obtained NiMo-Fe possesses high-efficiency OER performances. A low overpotential of 217 mV is required to achieve the current density of 10 mA cm^{-2}, which is 55 mV lower than that of the pre-catalyst without Mo species (donated as Ni-Fe). This work offers a new insight into the inactive-ion behavior and the ion effect on OER activity during OER process, which enlightens a promising pathway towards the designing of active and robust OER electrocatalysts.

2. Experimental section

2.1. Chemicals

Nickel-molybdenum foam (NiMo foam, atomic ratio of Ni/Mo = 17:3) and nickel foam (Ni foam) were purchased from Kunshan Guangjiayuan Electronic Co., Ltd. Iron chloride hexahydrate ($FeCl_3 \cdot 6H_2O$) and ruthenium oxide (RuO_2) were purchased from Aladdin Co., Ltd. Sodium chloride (NaCl), Hydrochloric acid (HCl), potassium hydroxide (KOH) and ethanol (C_2H_5OH) were purchased from Sinopharm Chemical Reagent Co., Ltd. Nafion perfluorinated resin solution (5 wt%) and Pt/C (Pt: 20% wt) were purchased from Sigma-Aldrich corporation. All chemicals are analytical grade and used as received without further purification. Ultrapure water (18.25 MΩ cm) was used throughout the whole experiments.

2.2. Synthesis of catalysts

A piece of rectangular NiMo foam with size of 1.5 * 0.5 cm^2 was washed respectively by 3.0 M of HCl solution, ultrapure water and ethanol for 10 min and dry. The treated NiMo foam as working electrode, a platinum (Pt) tablet as counter electrode and Ag/AgCl (saturated KCl) electrode as reference electrode were assembled in a three-electrode system. The electrolyte contained 30 mL of ultrapure water and 50 μL of 0.5 M $FeCl_3 \cdot 6H_2O$ solution (the experimental optimization is shown in Fig. S1). Then, an electrochemical treatment was carried out using cyclic voltammetric (CV) between 3.0 and −3.0 V for 40 cycles at a scan rate of 500 mV s^{-1} on a CHI660E electrochemical workstation. Subsequently, the electrode was cleaned with water and ethanol and then dried in air, which named as NiMo-Fe. Similarly, Ni-Fe was prepared through the treatment process with using the N foam as working electrode. NiMo and Ni were prepared via a similar electrochemical corrosion with NiMo foam and Ni foam as working electrode respectively in the electrolyte containing 30 mL of ultrapure water and 50 μL of 1 M NaCl solution.

2.3. Synthesis of NM-RuO₂

5 mg of RuO_2 powder was dispersed in a mixture containing 470 μL of ethanol and 30 μL of Nafion solution to form slurry. NM-RuO_2 was prepared by dipping the slurry onto a piece of NiMo foam with areal loading of 0.5 mg cm^{-2}.

2.4. Synthesis of Pt/C on Ni foam

Pt/C electrode was obtained through the similar method mentioned above with the addition of 5 mg Pt/C instead of RuO_2 with loading of 0.5 mg cm^{-2}.

2.5. Physical characterizations

Scanning electron microscopy (SEM) images were obtained on a Helios Nanolab 600i microscope. Transmission electron microscopy (TEM), high-resolution TEM (HRTEM) and energy-dispersive spectroscopy (EDS) images were taken on a FEI TF20 microscope coupled with EDS spectroscopy (Super-X). Atomic force microscope (AFM) was conducted on a Bruker Dimension ICON microscope to measure the thickness of catalyst. X-ray diffraction (XRD) patterns were collected on a Bruke D8 Advance X-ray diffraction system. X-ray photoelectron spectroscopy (XPS) spectra were recorded on a Thermo Scientific K-Alpha spectrometer. Raman spectra were acquired on a HORIBA LabRAM HR Evolution spectrometer under an excitation of 532 nm laser. The *in-situ* Raman spectra were collected under controlled potentials by the CHI 660E electrochemical workstation. The electrochemical operando Raman Cell is a H-type Cell (EC-RAIR-H). In addition, the working electrode is the as-obtained self-standing catalyst (N-F). A Pt foil used as the counter electrode and Ag/AgCl electrode (saturated KCl) used as the reference electrode. The *in-situ* Raman spectra were recorded under chronoamperometry from 0.1 to 0.9 V in 1.0 M KOH solution. Inductively coupled plasma-mass spectroscopy (ICP-MS) results were obtained from a ICAP 7000 SERIES spectrometer.

2.6. Electrochemical analysis

All the electrochemical measurements for OER were performed in a typical three-electrode cell in 1.0 M KOH connected to an electrochemical station (CHI 660E) at room temperature. An Ag/AgCl (saturated KCl) electrode and a Pt foil were used as the reference electrode and counter electrode, respectively. The as-prepared catalyst with exposed area of 1.0 * 0.5 cm^2 was used as the working electrode. All the potentials mentioned in this work were presented versus the reversible hydrogen electrode (RHE) according to the Nernst equation:

$$E_{RHE} = E_{Ag/AgCl} + 0.059 \times pH + 0.197 \ V$$

CV activation were performed for 25 cycles between 0.1 and 0.9 V at a scan rate of 50 mV s^{-1}. Polarization curves were *iR* compensated and collected in the range of 0.1–0.9 V with a scan rate of 5 mV s^{-1}. Overpotential was calculated based on the equation: η = E_{RHE} − 1.23 V. Electrochemical impedance spectroscopy (EIS) test was operated at the overpotential of 264 mV from 0.01 to 100, 000 Hz at the amplitude of 5 mV. Electrochemical surface area (ECSA) is positively correlated to the double-layered capacitor (C_{dl}), which was derived from the CV curves recorded in 0.1–0.2 V with scan rates of 20–100 mV s^{-1}. The overall water splitting in 1.0 M KOH was carried out by a two-electrode electrolyzer. Polarization curves were obtained in the range of 1.2–2.0 V at a scan rate of 5 mV s^{-1} with *iR* compensation. The long-term stability assessment was conducted on through chronopotentiometry (CP) measurement at a current density of 100 mA cm^{-2}.

2.7. Density functional theory (DFT) calculation

The theoretical investigations in this study are based on density functional theory, as performed in the Vienna ab initio simulation package (VASP) [36,37]. The exchange-correlation potential was obtained from the projected augmented wave (PAW) method by using Perdew-Burke- Ernzerhof (PBE) formula within the generalized gradient approximation (GGA) [38]. The cut-off energies for all calculations were set to be 500 eV. All the positions of atoms were fully relaxed until the

Hellmann-Feynman forces on each atom are less than 0.01 eV/Å. Meanwhile, a k-points Γ-centered mesh set was used for the Brillouin zone samples. The DFT-D3 method reported by Grimme was employed to describe the van der Waals interactions, which represents the chemisorption and physisorption properties on layered material. Furthermore, the Hubbard U correction was taken into account for the d electrons of Fe with U = 5.5 eV. A vacuum region of about 15 Å was used to decouple the periodic replicas. To evaluate the Gibbs free energy of intermediates (ΔG) on surface of catalyst (*) in four-electrons OER process, the following equations were adopted:

$$\Delta G_{OH*} = (E_{OH*} + 0.5 \times E_{H2} - E_{H2O} - E*) + (ZPE_{OH*} + 0.5 \times ZPE_{H2} - ZPE_{H2O} - ZPE*) - T \times (S_{OH*} + 0.5 \times S_{H2} - S_{H2O} - S*)$$

$$\Delta G_{O*} = (E_{O*} + E_{H2} - E_{H2O} - E*) + (ZPE_{O*} + ZPE_{H2} - ZPE_{H2O} - ZPE*) - T \times (S_{O*} + S_{H2} - S_{H2O} - S*)$$

$$\Delta G_{OOH*} = (E_{OOH*} + 1.5 \times E_{H2} - 2 \times E_{H2O} - E*) + (ZPE_{OOH*} + 1.5 \times ZPE_{H2} - 2 \times ZPE_{H2O} - ZPE*) - T \times (S_{OOH*} + 1.5 \times S_{H2} - 2 \times S_{H2O} - S*)$$

Where the E, ZPE, and S are stand for the total energy, zero-point energy and entropy of intermediates, respectively. The thermal energies of each intermediates were corrected at 298.15 K.

3. Results and discussion

3.1. Synthesis and characterizations of catalysts

The self-standing NiMo-Fe catalyst was synthesized via a one-step electrochemical strategy of CV cycles in $FeCl_3$ electrolyte using NiMo foam as working electrode (Fig. 1a). During the CV procedures, hydrogen evolution reaction can be occurred at cathode side, leading to an alkaline environment in electrolyte. The Fe^{3+} contained in electrolyte is able to deposit on the NiMo substrate via electrochemical deposition, while the metal Ni undergoes the electrochemical oxidation to form Ni$(OH)_2$ in the alkaline electrolyte. In the same way, Mo metal can be easily oxidized into MoO_4^{2-} in alkaline electrolyte according to the following equation: $Mo - 6e^- + 8OH^- = MoO_4^{2-} + 4H_2O$ [39]. In this case, the Fe can be successfully incorporated into the NiMo oxyhydroxide. To obtain the surface morphology of NiMo-Fe, SEM was performed. In contrast to the smooth surface of the initial NiMo foam (Fig. S2), the surface of NiMo-Fe becomes rough after electrochemical treating (Fig. S3), suggesting the successful fabrication of the NiMo-Fe layer on NiMo foam surface. The high-magnification SEM image (Fig. 1b) of NiMo-Fe reveals that the interconnected nanosheet arrays uniformly grow on substrate of NiMo foam to form a porous structure, which can be conducive to the electrolyte infiltration and oxygen output [40]. The control sample of Ni-Fe was prepared through the electrochemical treatment of Ni foam in a similar fashion. The SEM images (Fig. S4a-d) of N-F suggest the effective synthesis of the Ni-Fe layer on Ni foam surface in comparison to the SEM images of Ni foam (Fig. S4e-h). To shed light on the microscopic structure of NiMo-Fe, the TEM was carried out. As shown in TEM images (Fig. 1c and d), the ultrathin
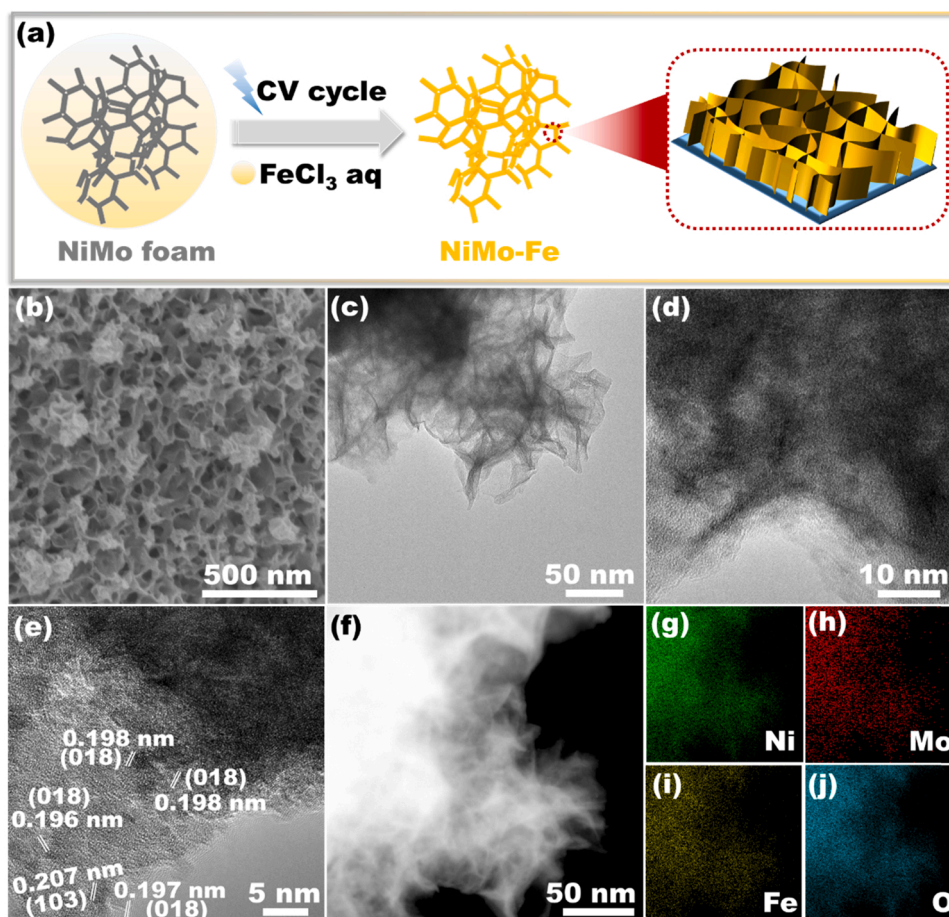

Fig. 1. a) Illustration of the synthesis of NiMo-Fe. b) SEM image of NiMo-Fe. c, d) TEM images of NiMo-Fe. e) HRTEM image of NiMo-Fe. f-j) EDS mapping of NiMo-Fe.

features of nanosheets can be clearly detected. The AFM image with the height profile in Fig. S5 further suggests the thickness of nanosheet is approximately 4 nm. In Fig. 1e, some lattice fringes on the edge and inside can be observed in the HRTEM image. The lattice spacings of 0.196, 0.197 and 0.198 nm are indexed to the (018) planes of α-Ni $(OH)_2$. Another lattice spacing of 0.207 nm is corresponded to the (103) plane of α-Ni(OH)$_2$ [41,42]. The EDS mapping images (Fig. 1f-j) demonstrate the homogeneous dispersity of Ni, Mo, Fe and O in NiMo-Fe. Furthermore, the contents of Ni, Mo and Fe (Fig. S6) are determined to be 26.59, 5.37 and 4.76 at%, respectively. According to these results, a hierarchical 3D framework of NiMo-Fe is successfully constructed on the surface of NiMo foam through the electrochemical treatment.

XRD and Raman spectroscopy were initially used to characterize the structures of NM-F and N-F. The XRD patterns of NiMo-Fe and Ni-Fe (Fig. S7) exhibit the nearly identical diffraction peaks of Ni foam. No any other diffraction peaks can be found due to the intense diffraction peaks of Ni foam substrate. Raman spectra (Fig. 2a) of NiMo-Fe and Ni-Fe show two obvious Raman peaks at around 450 and 527 cm^{-1}, which can be assigned to the Ni-O stretching vibration of α-Ni(OH)$_2$ and disordered structure of the Ni(OH)$_2$, respectively [43,44]. Noticeably, the adsorption peak at 527 cm^{-1} is also belonged to the Fe-O stretching mode of γ-FeOOH [45,46]. Compared with the Raman spectrum of NiMo (Fig. S8), the Fe—O bond appeared in NM-F indicates the successful incorporation of Fe. The peaks at 327 and 905 cm^{-1} in NiMo-Fe are indexed to the Mo-O stretching and bending modes of MoO_4^{2-}, respectively [47–49]. XPS was performed to investigate the surface oxidative states of catalysts. The survey XPS (Fig. S9) evidences the presences of Ni, Fe and Mo in NiMo-Fe. In Ni 2p XPS of NiMo-Fe (Fig. 2b), the peaks at 855.62 and 873.28 eV are attributed to the characterized peak of Ni^{2+} $2p_{3/2}$ and Ni^{2+} $2p_{1/2}$, respectively [50–52]. Two peaks at 232.32 eV (Mo^{6+} $3d_{5/2}$) and 235.45 eV (Mo^{6+} $3d_{3/2}$) in Mo 3d XPS (Fig. 2c) demonstrate the existence of Mo^{6+} in NiMo-Fe [53–55]. The Fe 2p XPS (Fig. 2d) shows well-defined peaks at around 710.84 and 724.45 eV, confirming the existence of Fe^{3+} [56,57]. The O 1s XPS (Fig. S10) of NiMo-Fe can be fitted into 529.73 eV of M-O, 531.09 eV of M-OH and 533.27 eV of H_2O, respectively [58,59]. The oxidative states of Ni, Fe and O in Ni-Fe were also analyzed by XPS (Fig. S11). The XPS results indicate that the oxidative states of Ni and Fe species are Ni^{2+} and Fe^{3+}, respectively. The O 1s XPS can be also deconvoluted to M-O, M-OH and H_2O, respectively.

More information about the electronic and coordinated structures of Fe and Mo in NiMo-Fe are obtained from X-ray absorption spectroscopy (XAS) at the Fe K-edge and Mo K-edge. The Fe K-edge X-ray absorption near-edge structure (XANES) spectra were exhibited in Fig. 2e. The adsorption edge of Fe K-edge from NiMo-Fe is closed to that of Fe_2O_3, further proving that the Fe^{3+} resides in NiMo-Fe [60]. In the spectra of Fourier transformed extended X-ray adsorption fine structure (FT-EXAFS) of Fe (Fig. 2f), the phase-uncorrected peak at about 1.6 Å represents the typical Fe—O bond in FeO_6 unit, and the peak at about 2.7 Å can be assigned to the Fe-M coordination between the neighbor FeO_6 unit [61–63]. With respect to Mo, the XANES and FT-XAFS spectra at Mo K-edge (Fig. S12) show that Mo is in both oxidized state and metallic state [40]. The above results demonstrate that the NiMo-Fe is composed of Fe incorporated NiMo oxyhydroxide.

3.2. OER performances of catalysts

The OER performances of NiMo-Fe and Ni-Fe were measured in 1.0 M KOH after CV activation. To exclude the effect of substrates, the OER activities of NiMo and Ni foam substrates were also measured. The polarization curves of NiMo-Fe and Ni-Fe (Fig. 3a) display the greatly enhanced catalytic activities in contrast to counterparts of pristine NiMo and Ni foam, respectively, suggesting that the OER activities comes from the NiMo-Fe and Ni-Fe catalytic layers rather than the original substrates. Impressively, the OER current of NiMo-Fe appears much earlier than that of Ni-Fe, revealing that the Mo species has a positive effect on the OER activity. Furthermore, the different samples of NiMo-Fe and Ni-Fe deliver outstanding reproducibility of OER performance in this work (Fig. S13). Fig. 3b displays the overpotentials to reach the current density of 10 mA cm^{-2} (η_{10}) and the corresponding Tafel slopes derived from the polarization curves of catalysts. The η_{10} of NiMo-Fe is 217 mV, which is much lower than those of Ni-Fe (272 mV), RuO_2 supported on NM foam (312 mV), NiMo foam (354 mV) and Ni foam (391 mV). And
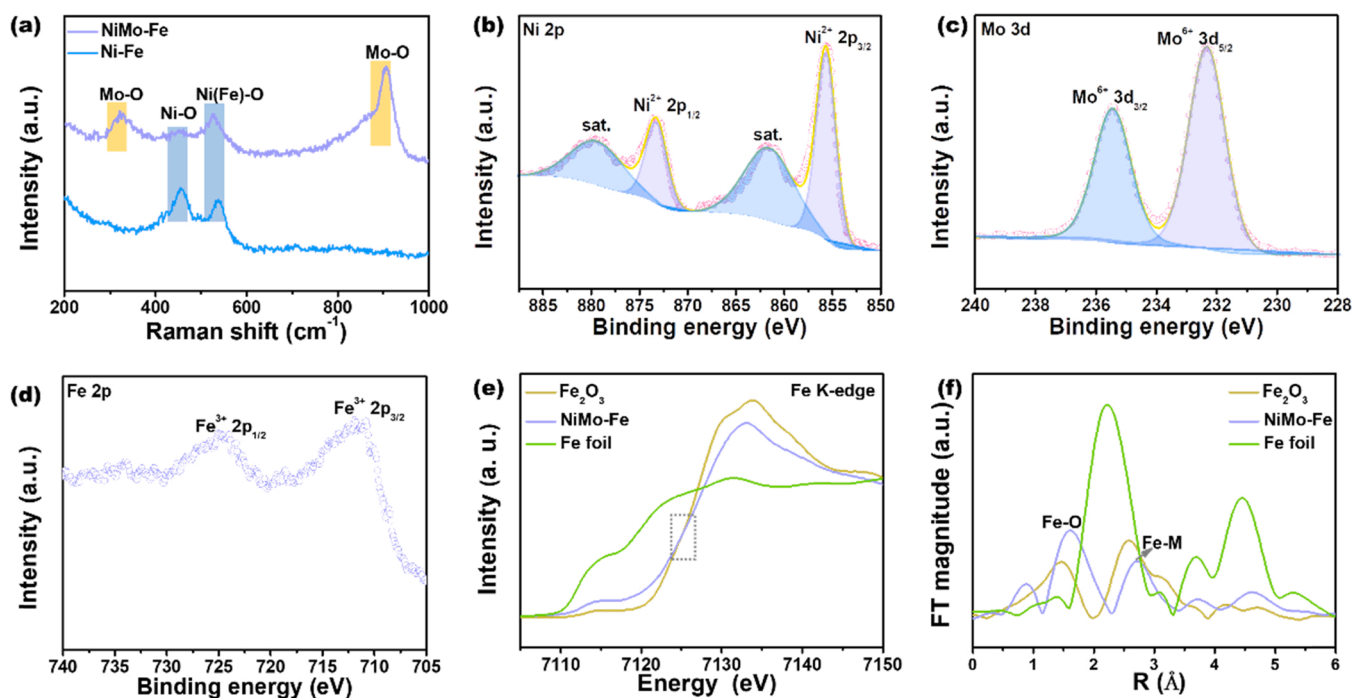

Fig. 2. a) Raman spectra of NiMo-Fe and Ni-Fe. High-resolution b) Ni 2p, c) Mo 3d and d) Fe 2p XPS of NiMo-Fe. e) XANES and f) FT-EXAFS at Fe K-edge of NiMo-Fe, Fe_2O_3 and Fe foil.
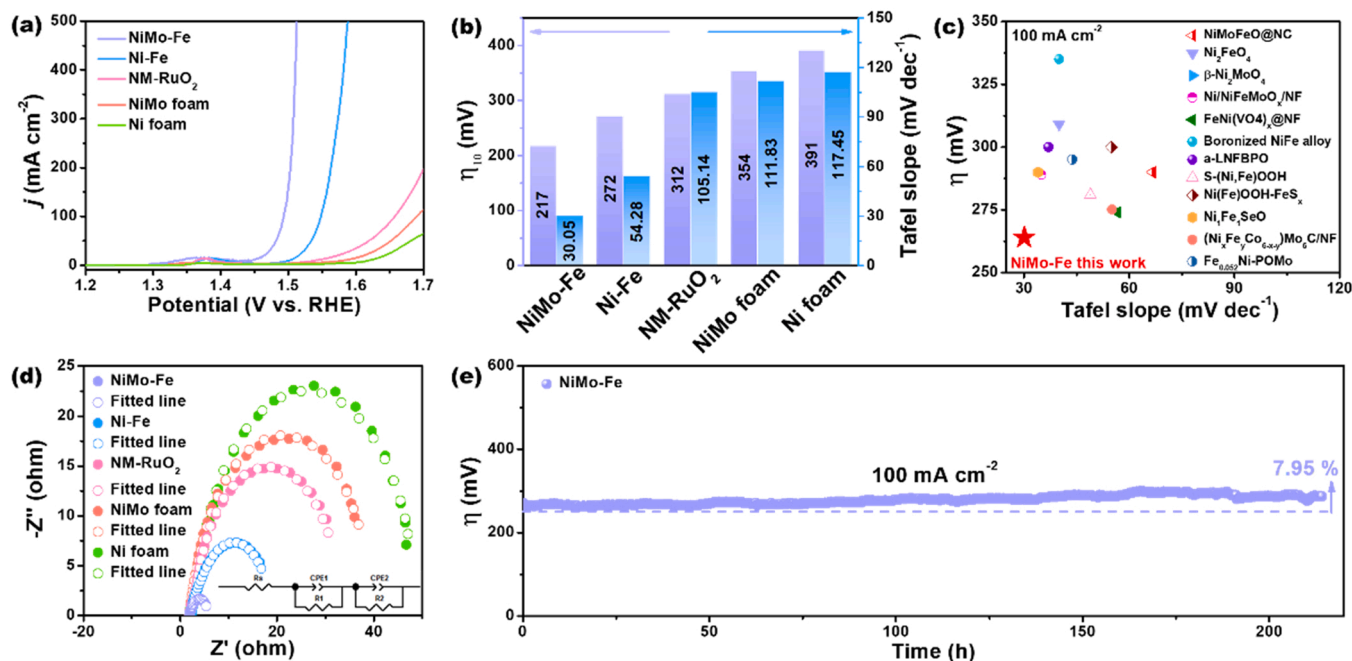
Fig. 3. a) Polarization curves of catalysts for OER. b) Overpotentials to reach the current density of 10 mA cm^{-2} and Tafel slopes of catalysts. c) Comparison of overpotentials to reach the current density of 100 mA cm^{-2} and Tafel slopes between NiMo-Fe and previously reported catalysts in alkaline OER. d) Fitted EIS plots of catalysts. Inset: relevant equilibrium circuit. e) Stability measurement of NiMo-Fe at a current of 100 mA cm^{-2}.

the Tafel slope of NiMo-Fe is determined to be 30.05 mV dec^{-1}, which is much smaller than those of Ni-Fe (54.28 mV dec^{-1}), NM-RuO$_2$ (105.14 mV dec^{-1}), NiMo foam (111.83 mV dec^{-1}) and Ni foam (117.45 mV dec^{-1}). The lowest Tafel slope of NiMo-Fe indicates its rapid OER kinetics. Such remarkable OER performances of NiMo-Fe enable it to compete with previously reported NiFe-based OER catalysts in alkaline media (Fig. 3c and Table S1). To further affirm the fastest OER kinetics of NiMo-Fe, the EIS was also measured (Fig. 3d). The parameters obtained from EIS fitting were listed in Table S2 using the equivalent circuit. The smallest charge-transfer resistance (R_{ct}) value (3.70 Ω) of NiMo-Fe indicates its speedy charge-transfer rate, which is agreed well with the results of Tafel slopes. To get rid of the possibility that the improved activity may be ascribed to the increase of catalyst's surface area, the intrinsic activities of NiMo-Fe and other control samples were normalized by ECSA, which is estimated by the C_{dl} derived from the CV curves in non-Faradaic region (Fig. S14a-e). From the normalized polarization curves in Fig. S14f, the NiMo-Fe shows a significantly enhanced OER activity compared with other control samples, suggesting the superior OER intrinsic activity of NiMo-Fe. This result demonstrates that the activity enhancement is not due to the increase of ECSA, but indeed results from the high intrinsic activity of NiMo-Fe.

In addition to the catalytic activity, the long-term stability is an important factor to estimate the OER performance of catalyst. CP measurement of NiMo-Fe was carried out at a current density of 100 mA cm^{-2}. As exhibited in Fig. 3e, the NiMo-Fe displays an excellent oxygen-evolution performance with a small overpotential-fluctuation of 7.95% over 200 h. Moreover, the polarization curve of NiMo-Fe shows slight delay after stability test (Fig. S15). To detect the morphology and structure of NiMo-Fe after stability test, SEM and TEM were performed (Fig. S16). SEM and TEM images suggest that the NiMo-Fe can retain its nanosheets structure after continuous oxygen evolution. HRTEM image and corresponding SAED pattern prove the formed amorphous structure of NiMo-Fe after stability test, suggesting a structural transformation of NiMo-Fe during the OER process. These results collectively demonstrate the satisfactory durability of NiMo-Fe during electrolysis.

To assess the potential of NiMo-Fe in large-scale hydrogen

production, a water electrolyzer was assembled employing NiMo-Fe and Pt/C (NiMo-Fe ‖ Pt/C) as anode and cathode, respectively. For comparison, the Ni-Fe paired with Pt/C (Ni-Fe ‖ Pt/C) and NM-RuO$_2$ paired with Pt/C (NM-RuO$_2$ ‖ Pt/C) were also fabricated. The water splitting activity was tested in 1.0 M KOH with 90% *iR* correction. As shown in Fig. S17a, the cell voltage of NiMo-Fe ‖ Pt/C required to achieve the current density of 10 mA cm^{-2} is 1.498 V, which is superior to those of Ni-Fe ‖ Pt/C (1.515 V) and NM-RuO$_2$ ‖ Pt/C (1.591 V). Furthermore, the NiMo-Fe ‖ Pt/C needs 1.555, 1.639 and 1.726 V to deliver the current densities of 50, 150 and 300 mA cm^{-2}, respectively, outperforms the Ni-Fe ‖ Pt/C and NM-RuO$_2$ ‖ Pt/C (Fig. S17b). Meanwhile, the NiMo-Fe ‖ Pt/C can work steadily at least 75 h at a high current density of 100 mA cm^{-2} (Fig. S17c), exhibiting a promising water splitting stability. The polarization curves of NiMo-Fe ‖ Pt/C are almost overlapped before and after stability measurement (Fig. S17d). On basis of above results, it can be concluded that the NiMo-Fe can be served as an effective OER catalyst.

3.3. Dynamic dissolution and re-adsorption of MoO_4^{2-}

To study the dynamic behavior of the MoO_4^{2-} in NiMo-Fe, the content of Mo in the electrolyte is analyzed by ICP-MS. In addition, the concentrations of Ni and Fe were also detected for comparison. The ICP-MS results in Fig. 4a indicate that Ni is hard to dissolve into the electrolyte and only trace amounts of Fe follow the dissolution and re-deposition trend. In contrast, there are small amount of Mo can be detected after CV activation, indicating that the Mo begins escaping from NiMo-Fe and dissolving into KOH solution. And the dissolution of MoO_4^{2-} causes an obvious structural collapse of NiMo-Fe, as evidenced by the SEM images in Fig. S18. NiMo-Fe still maintains its nanosheet structure despite the slight agglomeration. Interestingly, the concentration of Mo reaches the summit after 0.5 h for electrolysis and subsequently decreases to the nadir after OER measurement for 2 h, suggesting that the dissolved Mo perhaps re-adsorbs on surface of catalyst. Afterwards, the content of Mo increases and keeps at a relatively constant level with the incremental time of OER, possibly because of the equilibrium between the dissolution and re-adsorption of MoO_4^{2-}.
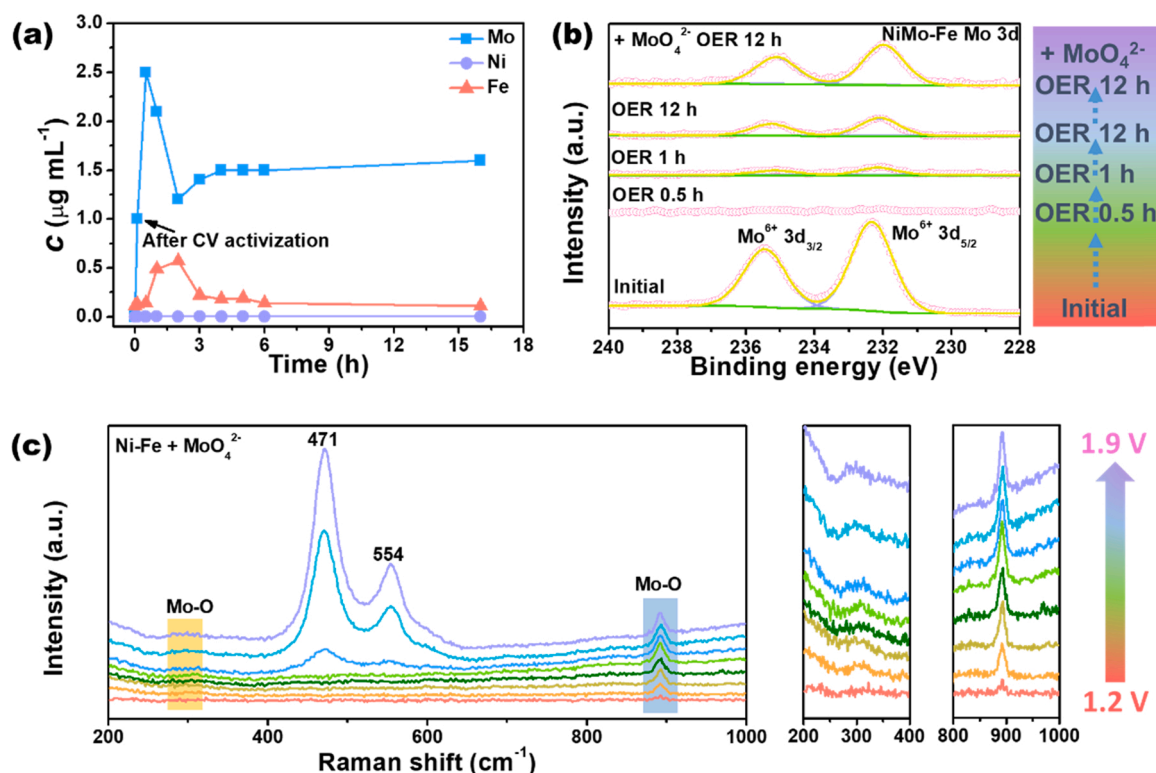
Fig. 4. a) Time-dependent concentration of dissolved Ni, Mo and Fe in the electrolyte of NiMo-Fe from ICP tests. b) High-resolution Mo 3d XPS of NiMo-Fe after 0.5 h, 1 h OER, 12 h OER in KOH and 12 h OER in MoO_4^{2-} contained KOH, respectively. c) Potential-dependent *in-situ* Raman spectra of Ni-Fe in MoO_4^{2-} contained KOH.

To confirm this assumption, the Mo 3d XPS of NiMo-Fe under various OER conditions were also measured. As shown in Fig. 4b, the signal of Mo^{6+} almost disappears after OER for 0.5 h, revealing the escape of the almost whole MoO_4^{2-} from NiMo-Fe into the electrolyte. Then, the intensity of Mo^{6+} peak occurs again after 1 h for OER and significantly increases after continuous OER for 12 h. Assisted by the added MoO_4^{2-} (0.1 M) in electrolyte, the XPS peak of can be further enhanced after OER for another 12 h. These results demonstrate that the escaped MoO_4^{2-} can be re-adsorbed on surface of NiMo-Fe. The negatively shifted XPS peaks of Mo^{6+} can be ascribed to the weakened Mo—O bonds during the dissolution and re-adsorption processes of MoO_4^{2-} [64]. The corresponding contents of Mo in NiMo-Fe from XPS results are displayed in Fig. S19, further confirming the dynamic dissolution and re-adsorption behavior of MoO_4^{2-} throughout OER process, which are corresponded well with the ICP-MS results (Fig. 4a).

To verify the re-adsorption of the dissolved MoO_4^{2-} under OER conditions, the potential dependent *in-situ* Raman spectra are also recorded of Ni-Fe with the addition of 0.1 M MoO_4^{2-} (Fig. S20). Both of the Mo-O stretching and bending modes come out with the existence of MoO_4^{2-}. In order to clearly observe the intensity changes of Mo-O vibration modes, the *in-situ* Raman spectra using the spectrum at 1.1 V as the baseline are exhibited in Fig. 4c. The intensity of Mo-O vibration modes shows an enhanced trend with an increased potential, demonstrating that the MoO_4^{2-} can undoubtedly be adsorbed on surface of Ni-Fe. Furthermore, a pair of peaks centered at 472 and 557 cm^{-1} appear initially at 1.7 V, which are indexed to the Ni-O bending and stretching modes of NiOOH, respectively [43,49,65]. The *ex-situ* Raman spectra of NiMo-Fe and Ni-Fe under different OER conditions are also shown in Fig. S21 and S22. The intensities of Mo-O vibration modes are reduced of NiMo-Fe after OER, but it can be enhanced again after adding extra MoO_4^{2-} in electrolyte. As for Ni-Fe, the Mo-O vibration modes can be distinctly identified with the addition of MoO_4^{2-}. The presence of Mo on surface of Ni-Fe is also detected by Mo 3d XPS and the content is about

0.56 at% (Fig. S23). Abovementioned results convincingly confirm the re-adsorption phenomenon of dissolved MoO_4^{2-} from NiMo-Fe during OER process. The trend of OER catalytic currents during the beginning hours of electrolysis are also investigated. The OER activities of NiMo-Fe are enhanced and finally maintain stable with the prolonged time of OER (Fig. S24). The overpotential decreases to nadir after 2 h for CP test, increases later and keeps stable in the CP curve (Fig. S25). These phenomena suggest that the dissolution and re-adsorption of MoO_4^{2-} contribute to the OER.

XPS and XAS were measured to investigate structural evolution of NiMo-Fe and Ni-Fe during OER process. In Fig. S26, the absorption peaks in Ni 2p XPS and Ni L-edge XAS both show a positive peak shift after OER for 12 h, implying the surface reconstruction of Ni^{2+} to Ni^{3+} in NiMo-Fe, which is consistent with the Raman results (Fig. S21) [60]. However, there is no obvious peak shift in Fe 2p XPS and Fe L-edge XAS (Figs. S27a, b) can be detected before and after OER process, suggesting that the Fe^{3+} in NiMo-Fe can maintain stable during OER process. Similarly, XANES of Fe K-edge (Fig. S27c) displays a good overlap during OER process, indicating that the valence of Fe^{3+} in NiMo-Fe is unchanged under OER conditions. The FT-EXAFS of Fe K-edge (Fig. S27d) shows a negative peak shift of Fe—O bond, indicating the generation of the shorter Fe—O bond, which is beneficial to capture OH^- during OER process [66,67]. The XANES and FT-EXAFS of Mo K-edge (Fig. S28) indicate the electronic and geometric structure of Mo species in NiMo-Fe without change during OER process. In O 1s XPS of NiMo-Fe after OER for 12 h (Fig. S29), the increased intensity of the M-O peak further manifests the transformation of $Ni(OH)_2$ to NiOOH [58]. These results evidence that the MoO_4^{2-} decorated Ni(Fe)OOH derived from the pre-catalyst (Fe incorporated NiMo oxyhydroxide) can be served as the active species for OER. The XPS results of Ni-Fe after OER similarly suggests the evolution of pre-catalyst to an active phase of Ni(Fe)OOH (Fig. S30). In addition, the structural stability of NiMo-Fe after durability test was analyzed. XRD pattern, Raman and XPS spectra (Fig. S31)

prove that the active species of MoO_4^{2-} decorated Ni(Fe)OOH is highly stable during continuous oxygen evolution.

3.4. Promoting effect of MoO_4^{2-} on OER performance

To explore the role of MoO_4^{2-} on OER performance, the CV curves of NiMo-Fe and Ni-Fe are compared in Fig. 5a to investigate their redox behaviors. The redox peaks can be ascribed to the reconstruction process of $Ni^{2+} \rightarrow Ni^{3+} \rightarrow Ni^{2+}$. For NiMo-Fe, the area of the closed curves increases gradually, and is much higher than that of the Ni-Fe, revealing a higher reconstruction degree of NiMo-Fe. The result indicates that the dissolution of MoO_4^{2-} is able to improve the reconstruction degree from the pre-catalyst to active species [29,68,69]. To investigate the effect of re-adsorbed MoO_4^{2-} on OER performance, the polarization curves of NiMo-Fe were collected in the initial KOH electrolyte, renewed KOH electrolyte and KOH electrolyte with 0.05 M MoO_4^{2-}, respectively. As displayed in Fig. 5b, the OER activity of NiMo-Fe decays after renewing the KOH electrolyte, indicating that the dissolved MoO_4^{2-} plays an important contribution to the OER activity. Importantly, the OER activity of NiMo-Fe is recovered and enhanced after adding 0.05 M MoO_4^{2-} in KOH. The η_{10} (200 mV) is 17 mV lower than the pristine NiMo-Fe, revealing that the MoO_4^{2-} delivers a promoting effect on OER activity. The positive effect of MoO_4^{2-} on OER is universal to Ni-Fe. The CV curves in Fig. S32 indicate that the additional MoO_4^{2-} has no obvious effect on the reconstruction of Ni-Fe. The catalytic activity of Ni-Fe is boosted by the adsorption of MoO_4^{2-} under OER conditions (Fig. 5c). With the optimum concentration (0.05 M) of MoO_4^{2-}, the η_{10} of Ni-Fe is 250 mV, which is 22 mV lower than that of Ni-Fe in pure KOH electrolyte.

And the corresponding Tafel slope also decreases from 54.28 to 46.4 mV dec^{-1}, showing an accelerated OER kinetics. EIS plots in Fig. 5d show the contractible radius of the semicircle with the added MoO_4^{2-}, indicating that the MoO_4^{2-} is capable of expediting the charge transfer process. The slightly decreased C_{dl} values of Ni-Fe with MoO_4^{2-} suggest that the accelerated OER activity is rooted in the increased intrinsic activity, rather than the ECSA (Fig. S33). With the addition of MoO_4^{2-}, the Ni-Fe presents a steady oxygen evolution output (Fig. S34). All results demonstrate the dissolved and re-adsorbed MoO_4^{2-} is able to contribute high activity in NiMo-Fe toward OER.

Furthermore, DFT calculations were carried out to understand the promoted effect of MoO_4^{2-} on OER activity. The results of *in-situ* Raman, ICP and XPS detects the reconstruction of forming NiOOH accompanied with the dissolution and re-adsorption of MoO_4^{2-} (Fig. 4). The MoO_4^{2-} decorated NiOOH does not contribute to the OER directly, but can serves as an ideal host for Fe incorporation as reported by previous studies [70, 71]. The differences in Raman spectra of NiMo-Fe and NiMo (Fig. S8) reveal the successful incorporation of Fe into the NiMo oxyhydroxide host [45,46]. The negatively shifted anodic peaks of NiMo-Fe compared with that of NiMo in CV curves further demonstrate the impact of incorporated Fe on redox behaviors (Fig. S35) [72]. Therefore, the MoO_4^{2-} decorated Ni(Fe)OOH is deemed as the real active phase for OER. Firstly, the free energies of MoO_4^{2-} adsorbed on Ni and Fe site are compared in Fig. 6a. The adsorption energy of MoO_4^{2-} on Ni site is 1.52 eV lower than that on Fe site, revealing that the MoO_4^{2-} prefers to adsorb on Ni site. Therefore, the structural models of Ni(Fe)OOH-MoO$_4$ and Ni(Fe)OOH with the Fe site was established (Fig. S36). Furthermore, the structural model of NiOOH with the Ni site was built to compare the activity of Ni and Fe sites. The Gibbs free energies of the OER intermediates (OH*, O* and OOH*) were calculated as shown in Fig. 6b. Compared to pure NiOOH and Ni(Fe)OOH, Ni(Fe)OOH-MoO$_4$ show lower Gibbs free energies ($\triangle$G) of the potential-determining step (PDS),
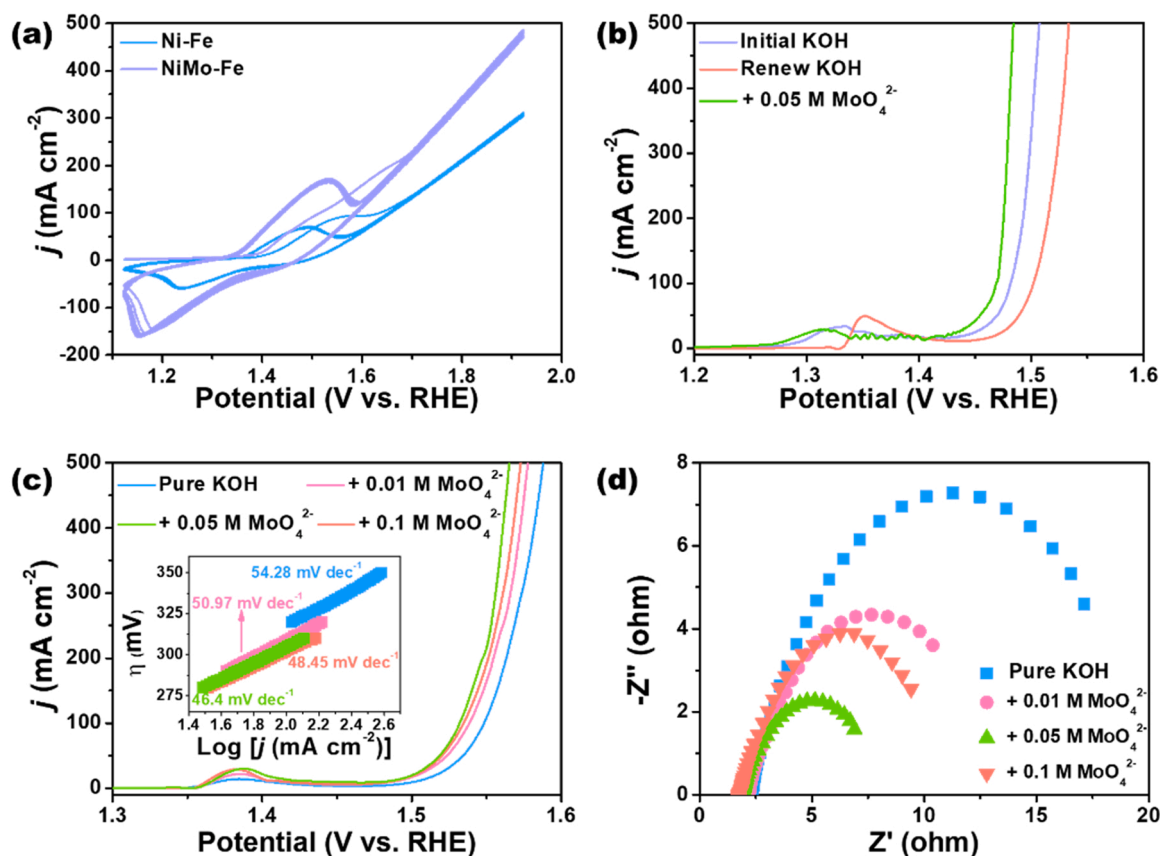

Fig. 5. a) CV curves of NiMo-Fe and Ni-Fe in range of 0.1–0.9 V at scan rate of 50 mV s^{-1}. b) Polarization curves of NiMo-Fe in the initial KOH, renewed KOH and MoO_4^{2-} contained KOH, respectively. c) Polarization curves (Inset: the corresponding Tafel slopes) and d) EIS plots of Ni-Fe in KOH after adding MoO_4^{2-} with different concentrations.
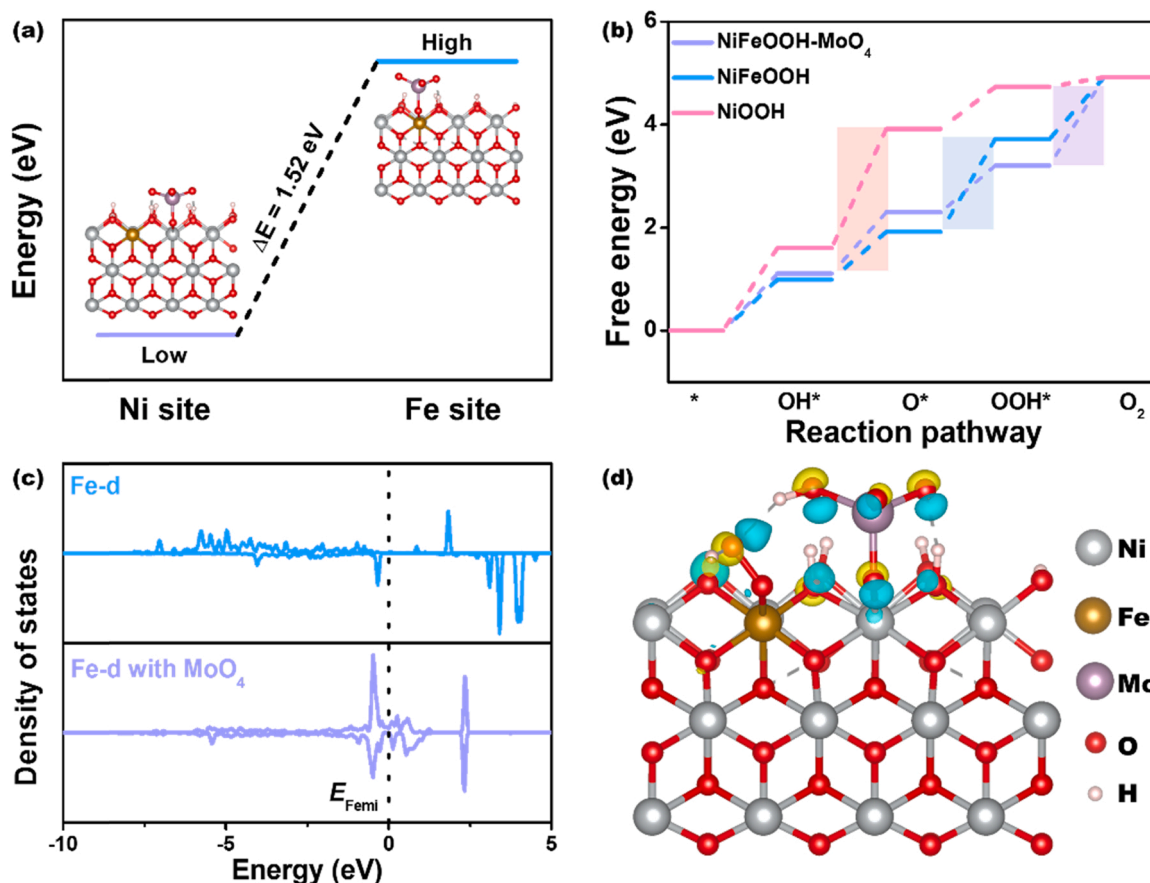
Fig. 6. a) Adsorption energy of MoO_4^{2-} on Ni and Fe site of Ni(Fe)OOH. b) Gibbs free energy profiles of OER intermediates over NiOOH, Ni(Fe)OOH and Ni(Fe)OOH-MoO_4. c) DOS of Fe 3d orbitals in Ni(Fe)OOH and Ni(Fe)OOH-MoO_4. d) Differential charge densities of Ni(Fe)OOH-MoO_4 when OOH* is adsorbed on the Fe site (Yellow and blue counters stand for electron accumulation and depletion, respectively). (For interpretation of the references to color in this figure legend, the reader is referred to the web version of this article.)

suggesting that the OER occurred on Fe site is more easily than that on Ni site, which demonstrates that the Fe site is the active site. As displayed in Fig. S37, introducing Fe can greatly enhance the OER performances of NiMo and Ni, further indicating the higher activity of Fe site [71,73–75]. For Ni(Fe)OOH, the PDS on Fe site is the transformation of O* to OOH* owing to the large difference between $\triangle G_{O*}$ and $\triangle G_{OOH*}$. With the modification of MoO_4^{2-} on surface of catalyst (Ni(Fe)OOH-MoO_4), the PDS is changed and all the $\triangle G$ are decreased. Moreover, the density of state (DOS) (Fig. 6c) reveals the enhanced electron density around the Fermi level of Fe 3d orbital in Ni(Fe)OOH-MoO_4 in contrast to the bare Ni(Fe)OOH, which performs an improved electron transfer capability and a stronger bonding with the adsorbates [76,77]. The effect of MoO_4^{2-} on electron modulation is also researched by the differential charge density. As shown in Fig. S38, the OH* and O* have a small amount of charge redistribution. On the contrary, it is clear that the OOH* intermediate on Fe site exhibits more significant electron accumulation (Fig. 6d), which indicates that the MoO_4^{2-} is more favorable for the adsorption of OOH* than OH* and O* [78]. DFT calculations confirm that the re-adsorbed MoO_4^{2-} is able to enhance the adsorption of the OOH* intermediate adsorbed on Fe site, thus decreases the $\triangle G$ and improves the OER activity.

4. Conclusion

In summary, the dynamic re-adsorption behavior of the escaped MoO_4^{2-} from the pre-catalyst during OER process is discovered, which can mediate an enhanced activity for electrocatalytic OER. The results of ICP-OES, XPS and *in-situ* Raman reveal that the MoO_4^{2-} in NiMo-Fe can

be dissolved and re-adsorbed on the surface of catalyst under OER condition. The CV curves probe that the reconstruction degree of NiMo-Fe to active species can be enhanced by the dissolution of MoO_4^{2-}. And LSV curves in MoO_4^{2-} contained electrolyte confirm that the MoO_4^{2-} plays a positive effect on catalytic activity. Adding appropriate MoO_4^{2-} can enhance the catalytic activity of NiMo-Fe and Ni-Fe. DFT calculations demonstrate that the re-adsorbed MoO_4^{2-} can improve the OER activity by facilitating the adsorption of the OOH* intermediate. As results, the as-obtained NiMo-Fe presents an enhanced OER performance compared to N-F. It only a low η_{10} of 217 mV with a small Tafel slope of 30.05 mV dec^{-1} and possesses a high stability over 200 h at current density of 100 mA cm^{-2}. This work uncovers the neglected re-adsorption phenomenon of the dissolved MoO_4^{2-} from NiMo-Fe and demonstrates the promoting effect of re-adsorbed MoO_4^{2-} on OER activity, thus may providing a paradigm for the adsorption-modulated electrocatalysts toward other energy storage and conversion devices.

Author statement

The manuscript was written through contributions of all authors. All authors have given approval to the final version of the manuscript. Jun Pan, Min Liu and Pengfei Tan supervised the project. Hanxiao Liao and Kejun Chen designed the study and generated the figures. Xiaodong Zhang conducted the DFT calculations. Gongming Wang and Shuwen Niu measured the Raman spectroscopy measurements. Yong Liu helped with obtaining SEM images.

Declaration of Competing Interest

The authors declare that they have no known competing financial interests or personal relationships that could have appeared to influence the work reported in this paper.

Acknowledgment

Appendix A. Supporting information

Supplementary data associated with this article can be found in the online version at doi:10.1016/j.apcatb.2022.121150.

References

[1] D. Liu, A. Barbar, T. Najam, M.S. Javed, J. Shen, P. Tsiakaras, X. Cai, Single noble metal atoms doped 2D materials for catalysis, Appl. Catal. B Environ. 297 (2021), 120389.

[2] D. Zhao, Z. Zhuang, X. Cao, C. Zhang, Q. Peng, C. Chen, Y. Li, Atomic site electrocatalysts for water splitting, oxygen reduction and selective oxidation, Chem. Soc. Rev. 49 (2020) 2215–2264.

[3] J. Huang, H. Sheng, R.D. Ross, J. Han, X. Wang, B. Song, S. Jin, Modifying redox properties and local bonding of Co_3O_4 by CeO_2 enhances oxygen evolution catalysis in acid, Nat. Commun. 12 (2021) 3036.

[4] F. Du, X. Ling, Z. Wang, S. Guo, Y. Zhang, H. He, G. Li, C. Jiang, Y. Zhou, Z. Zou, Strained heterointerfaces in sandwich-like NiFe layered double hydroxides/$Co_{1-x}S$ for highly efficient and superior long-term durable oxygen evolution reaction, J. Catal. 389 (2020) 132–139.

[5] S.-Y. Lee, I.-S. Kim, H.-S. Cho, C.-H. Kim, Y.-K. Lee, Resolving potential-dependent degradation of electrodeposited $Ni(OH)_2$ catalysts in alkaline oxygen evolution reaction (OER): in situ XANES studies, Appl. Catal. B Environ. 284 (2021), 119729.

[6] A. Bergmann, T.E. Jones, E.M. Moreno, D. Teschner, P. Chernev, M. Gliech, T. Reier, H. Dau, P. Strasser, Unified structural motifs of the catalytically active state of Co (oxyhydr) oxides during the electrochemical oxygen evolution reaction, Nat. Catal. 1 (2018) 711–719.

[7] M.W. Kanan, D.G. Nocera, In situ formation of an oxygen-evolving catalyst in neutral water containing phosphate and Co^{2+}, Science 321 (2008) 1072–1075.

[8] Z.-F. Huang, J. Song, Y. Du, S. Xi, S. Dou, J.M.V. Nsanzimana, C. Wang, Z.J. Xu, X. Wang, Chemical and structural origin of lattice oxygen oxidation in Co-Zn oxyhydroxide oxygen evolution electrocatalysts, Nat. Energy 4 (2019) 329–338.

[9] Z. Xiao, Y.-C. Huang, C.-L. Dong, C. Xie, Z. Liu, S. Du, W. Chen, D. Yan, L. Tao, Z. Shu, G. Zhang, H. Duan, Y. Wang, Y. Zou, R. Chen, S. Wang, Operando identification of the dynamic behavior of oxygen vacancy-rich Co_3O_4 for oxygen evolution reaction, J. Am. Chem. Soc. 142 (2020) 12087–12095.

[10] Y. Luo, Z. Zhang, F. Yang, J. Li, Z. Liu, W. Ren, B. Liu, Stabilized hydroxide-mediated nickel-based electrocatalysts for high-current-density hydrogen evolution in alkaline media, Energy Environ. Sci. 14 (8) (2021) 4010–4619.

[11] X.-P. Li, C. Huang, W.-K. Han, T. Ouyang, Z.-Q. Liu, Transition metal-based electrocatalysts for overall water splitting, Chin. Chem. Lett. 32 (2021) 2597–2616.

[12] M. Gong, Y. Li, H. Wang, Y. Liang, J.Z. Wu, J. Zhou, J. Wang, T. Regier, F. Wei, H. Dai, An advanced Ni-Fe layered double hydroxide electrocatalyst for water oxidation, J. Am. Chem. Soc. 135 (2013) 8452–8455.

[13] H.Y. Wang, Y.Y. Hsu, R. Chen, T.S. Chan, H.M. Chen, B. Liu, Ni^{3+}-induced formation of active NiOOH on the spinel Ni-Co oxide surface for efficient oxygen evolution reaction, Adv. Energy Mater. 5 (2015) 1500091.

[14] L. Xu, Q. Jiang, Z. Xiao, X. Li, J. Huo, S. Wang, L. Dai, Plasma-engraved Co_3O_4 nanosheets with oxygen vacancies and high surface area for the oxygen evolution reaction, Angew. Chem. Int. Ed. 55 (2016) 5277–5281.

[15] X. Liu, F. Xia, R. Guo, M. Huang, J. Meng, J. Wu, L. Mai, Ligand and anion Co-leaching induced complete reconstruction of polyoxomolybdate-organic complex oxygen-evolving pre-catalysts, Adv. Funct. Mater. 31 (2021) 2101792.

[16] W.-K. Han, X.-P. Li, L.-N. Lu, T. Ouyang, K. Xiao, Z.-Q. Liu, Partial S substitution activates $NiMoO_4$ for efficient and stable electrocatalytic urea oxidation, Chem. Commun. 56 (2020) 11038–11041.

[17] T. Ouyang, X.-T. Wang, X.-Q. Mai, A.-N. Chen, Z.-Y. Tang, Z.-Q. Liu, Coupling magnetic single-crystal $Co_2Mo_3O_8$ with ultrathin nitrogen-rich carbon layer for oxygen evolution reaction, Angew. Chem. Int. Ed. 59 (2020) 11948–11957.

[18] C. Wang, H. Yang, Y. Zhang, Q. Wang, NiFe alloy nanoparticles with hcp crystal structure stimulate superior oxygen evolution reaction electrocatalytic activity, Angew. Chem. Int. Ed. 58 (2019) 6099–6103.

[19] W. Cai, R. Chen, H. Yang, H.B. Tao, H.-Y. Wang, J. Gao, W. Liu, S. Liu, S.-F. Hung, B. Liu, Amorphous versus crystalline in water oxidation catalysis: a case study of NiFe alloy, Nano Lett. 20 (2020) 4278–4285.

[20] X. Yu, P. Yang, S. Chen, M. Zhang, G. Shi, NiFe alloy protected silicon photoanode for efficient water splitting, Adv. Energy Mater. 7 (2017) 1601805.

[21] W. Zhou, X.-J. Wu, X. Cao, X. Huang, C. Tan, J. Tian, H. Liu, J. Wang, H. Zhang, Ni_3S_2 nanorods/Ni foam composite electrode with low overpotential for electrocatalytic oxygen evolution, Energy Environ. Sci. 6 (2013) 2921–2924.

[22] Y. Liu, H. Cheng, M. Lyu, S. Fan, Q. Liu, W. Zhang, Y. Zhi, C. Wang, C. Xiao, S. Wei, Low overpotential in vacancy-rich ultrathin $CoSe_2$ nanosheets for water oxidation, J. Am. Chem. Soc. 136 (2014) 15670–15675.

[23] C. Tang, N. Cheng, Z. Pu, W. Xing, X. Sun, NiSe nanowire filmsupported on nickel foam: an efficient and stable 3D bifunctional electrode for full water splitting, Angew. Chem. Int. Ed. 54 (2015) 9351–9355.

[24] Z. Chen, R. Zheng, M. Graś, W. Wei, G. Lota, H. Chen, B.-J. Ni, Tuning electronic property and surface reconstruction of amorphous iron borides via WP co-doping for highly efficient oxygen evolution, Appl. Catal. B Environ. 288 (2021), 120037.

[25] Z.J. Chen, T. Zhang, X.Y. Gao, Y.J. Huang, X.H. Qin, Y.F. Wang, K. Zhao, X. Peng, C. Zhang, L. Liu, Engineering microdomains of oxides in high-entropy alloy electrodes toward efficient oxygen evolution, Adv. Mater. (2021) 2101845.

[26] E. Fabbri, M. Nachtegaal, T. Binninger, X. Cheng, B.-J. Kim, J. Durst, F. Bozza, T. Graule, R. Schäublin, L. Wiles, Dynamic surface self-reconstruction is the key of highly active perovskite nano-electrocatalysts for water splitting, Nat. Mater. 16 (2017) 925–931.

[27] J. Chen, Q. Long, K. Xiao, T. Ouyang, N. Li, S. Ye, Z.-Q. Liu, Vertically-interlaced NiFeP/MXene electrocatalyst with tunable electronic structure for high-efficiency oxygen evolution reaction, Sci. Bull. 66 (2021) 1063–1072.

[28] Y. Wang, Y. Zhu, S. Zhao, S. She, F. Zhang, Y. Chen, T. Williams, T. Gengenbach, L. Zu, H. Mao, W. Zhou, Z. Shao, H. Wang, J. Tang, D. Zhao, C. Selomulya, Anion etching for accessing rapid and deep self-reconstruction of precatalysts for water oxidation, Matter 3 (2020) 2124–2137.

[29] X. Liu, J. Meng, K. Ni, R. Guo, F. Xia, J. Xie, X. Li, B. Wen, P. Wu, M. Li, J. Wu, X. Wu, L. Mai, D. Zhao, Complete reconstruction of hydrate pre-catalysts for ultrastable water electrolysis in industrial-concentration alkali media, Cell Rep. Phys. Sci. 1 (2020), 100241.

[30] X. Wang, X. Sang, C.L. Dong, S. Yao, L. Shuai, J. Lu, B. Yang, Z. Li, L. Lei, M. Qiu, Proton capture strategy for enhancing electrochemical CO_2 reduction on atomically dispersed metal-nitrogen active sites, Angew. Chem. Int. Ed. 60 (2021) 11959–11965.

[31] F. Pan, H. Zhang, Z. Liu, D. Cullen, K. Liu, K. More, G. Wu, G. Wang, Y. Li, Atomic-level active sites of efficient imidazolate framework-derived nickel catalysts for CO_2 reduction, J. Mater. Chem. A 7 (2019) 26231–26237.

[32] Z. Zhang, L. Melo, R.P. Jansonius, F. Habibzadeh, E.R. Grant, C.P. Berlinguette, pH matters when reducing CO_2 in an electrochemical flow cell, ACS Energy Lett. 5 (2020) 3101–3107.

[33] C.-T. Dinh, T. Burdyny, M.G. Kibria, A. Seifitokaldani, C.M. Gabardo, F.P.G. De Arquer, A. Kiani, J.P. Edwards, P. De Luna, O.S. Bushuyev, CO_2 electroreduction to ethylene via hydroxide-mediated copper catalysis at an abrupt interface, Science 360 (2018) 783–787.

[34] S. Ringe, E.L. Clark, J. Resasco, A. Walton, B. Seger, A.T. Bell, K. Chan, Understanding cation effects in electrochemical CO_2 reduction, Energy Environ. Sci. 12 (2019) 3001–3014.

[35] J. Resasco, L.D. Chen, E. Clark, C. Tsai, C. Hahn, T.F. Jaramillo, K. Chan, A.T. Bell, Promoter effects of alkali metal cations on the electrochemical reduction of carbon dioxide, J. Am. Chem. Soc. 139 (2017) 11277–11287.

[36] G. Kresse, J. Hafner, Ab initio molecular dynamics for liquid metals, Phys. Rev. B 47 (1993) 558–561.

[37] G. Kresse, J. Furthmüller, Efficient iterative schemes for ab initio total-energy calculations using a plane-wave basis set, Phys. Rev. B 54 (1996) 11169–11186.

[38] J.P. Perdew, K. Burke, M. Ernzerhof, Generalized gradient approximation made simple, Phys. Rev. Lett. 77 (1996) 3865–3868.

[39] M. deKay Thompson, A.L. Kaye, The electrochemical oxidation of molybdenum in potassium hydroxide solutions, Trans. Electrochem. Soc. 62 (1932) 255.

[40] Y. Luo, Z. Zhang, F. Yang, J. Li, Z. Liu, W. Ren, S. Zhang, B. Liu, Stabilized hydroxide-mediated nickel-based electrocatalysts for high-current-density hydrogen evolution in alkaline media, Energy Environ. Sci. 14 (2021) 4610–4619.

[41] H. Wang, J. Gao, Z. Li, Y. Ge, K. Kan, K. Shi, One-step synthesis of hierarchical α-Ni $(OH)_2$ flowerlike architectures and their gas sensing properties for NO_x at room temperature, CrystEngComm 14 (2012) 6843–6852.

[42] D. Shi, L. Zhang, N. Zhang, Z.-Y. Zhang, Z.G. Yu, H. Gong, Boosted electrochemical properties from the surface engineering of ultrathin interlaced $Ni(OH)_2$ nanosheets with $Co(OH)_2$ quantum dot modification, Nanoscale 10 (2018) 10554–10563.

[43] M.W. Louie, A.T. Bell, An investigation of thin-film Ni-Fe oxide catalysts for the electrochemical evolution of oxygen, J. Am. Chem. Soc. 135 (2013) 12329–12337.

[44] H.B. Li, M.H. Yu, F.X. Wang, P. Liu, Y. Liang, J. Xiao, C.X. Wang, Y.X. Tong, G. W. Yang, Amorphous nickel hydroxide nanospheres with ultrahigh capacitance and energy density as electrochemical pseudocapacitor materials, Nat. Commun. 4 (2013) 1894.

[45] M.K. Nieuwoudt, J.D. Comins, I. Cukrowski, The growth of the passive film on iron in 0.05 M NaOH studied in situ by Raman micro-spectroscopy and electrochemical polarisation. Part I: near-resonance enhancement of the Raman spectra of iron oxide and oxyhydroxide compounds, J. Raman Spectrosc. 42 (2011) 1335–1339.

[46] T. Nguyen, M. Fátima Montemor, γ-FeOOH and amorphous Ni-Mn hydroxide on carbon nanofoam paper electrodes for hybrid supercapacitors, J. Mater. Chem. A 6 (2018) 2612–2624.

[47] X. Liu, R. Guo, K. Ni, F. Xia, C. Niu, B. Wen, J. Meng, P. Wu, J. Wu, X. Wu, Reconstruction-Determined Alkaline Water Electrolysis at Industrial Temperatures, Adv. Mater. 32 (2020) 2001136.

[48] C. Xie, Y. Wang, K. Hu, L. Tao, X. Huang, J. Huo, S. Wang, In situ confined synthesis of molybdenum oxide decorated nickel-iron alloy nanosheets from MoO_4^{2-} intercalated layered double hydroxides for the oxygen evolution reaction, J. Mater. Chem. A 5 (2017) 87–91.

[49] J. Choi, D. Kim, W. Zheng, B. Yan, Y. Li, L.Y.S. Lee, Y. Piao, Interface engineered $NiFe_2O_{4-x}/NiMoO_4$ nanowire arrays for electrochemical oxygen evolution, Appl. Catal. B Environ. 286 (2021) 119857.

[50] J. Liu, W. Cheng, F. Tang, H. Su, Y. Huang, F. Hu, X. Zhao, Y. Jiang, Q. Liu, S. Wei, Electron delocalization boosting highly efficient electrocatalytic water oxidation in layered hydrotalcites, J. Phys. Chem. C 121 (2017) 21962–21968.

[51] T. Wang, G. Nam, Y. Jin, X. Wang, P. Ren, M.G. Kim, J. Liang, X. Wen, H. Jang, J. Han, NiFe (Oxy) hydroxides derived from NiFe disulfides as an efficient oxygen evolution catalyst for rechargeable Zn-air batteries: the effect of surface S residues, Adv. Mater. 30 (2018) 1800757.

[52] Y. Zhao, Y. Gao, Z. Chen, Z. Li, T. Ma, Z. Wu, L. Wang, Trifle Pt coupled with NiFe hydroxide synthesized via corrosion engineering to boost the cleavage of water molecule for alkaline water-splitting, Appl. Catal. B Environ. 297 (2021), 120395.

[53] X. Wang, R. Su, H. Aslan, J. Kibsgaard, S. Wendt, L. Meng, M. Dong, Y. Huang, F. Besenbacher, Tweaking the composition of NiMoZn alloy electrocatalyst for enhanced hydrogen evolution reaction performance, Nano Energy 12 (2015) 9–18.

[54] W. Du, Y. Shi, W. Zhou, Y. Yu, B. Zhang, Unveiling the in situ dissolution and polymerization of Mo in Ni_4Mo alloy for promoting the hydrogen evolution reaction, Angew. Chem. Int. Ed. 60 (2021) 7051–7055.

[55] Z. Dai, F. Qin, H. Zhao, J. Ding, Y. Liu, R. Chen, Crystal defect engineering of aurivillius Bi_2MoO_6 by Ce doping for increased reactive species production in photocatalysis, ACS Catal. 6 (2016) 3180–3192.

[56] C. Zhang, M. Shao, L. Zhou, Z. Li, K. Xiao, M. Wei, Hierarchical NiFe layered double hydroxide hollow microspheres with highly-efficient behavior toward oxygen evolution reaction, ACS Appl. Mater. Interfaces 8 (2016) 33697–33703.

[57] C.-X. Zhao, J.-N. Liu, J. Wang, D. Ren, J. Yu, X. Chen, B.-Q. Li, Q. Zhang, A ΔE = 0.63 V bifunctional oxygen electrocatalyst enables high-rate and long-cycling zinc-air batteries, Adv. Mater. 33 (2021) 2008606.

[58] Y. Wang, Y. Zhu, S. Zhao, S. She, F. Zhang, Y. Chen, T. Williams, T. Gengenbach, L. Zu, H. Mao, Anion etching for accessing rapid and deep self-reconstruction of precatalysts for water oxidation, Matter 3 (2020) 2124–2137.

[59] H. Yang, L. Gong, H. Wang, C. Dong, J. Wang, K. Qi, H. Liu, X. Guo, B.Y. Xia, Preparation of nickel-iron hydroxides by microorganism corrosion for efficient oxygen evolution, Nat. Commun. 11 (2020), 5075.

[60] J. Jiang, F. Sun, S. Zhou, W. Hu, H. Zhang, J. Dong, Z. Jiang, J. Zhao, J. Li, W. Yan, Atomic-level insight into super-efficient electrocatalytic oxygen evolution on iron and vanadium co-doped nickel (oxy) hydroxide, Nat. Commun. 9 (2018), 2885.

[61] D. Friebel, M.W. Louie, M. Bajdich, K.E. Sanwald, Y. Cai, A.M. Wise, M.-J. Cheng, D. Sokaras, T.-C. Weng, R. Alonso-Mori, Identification of highly active Fe sites in (Ni, Fe) OOH for electrocatalytic water splitting, J. Am. Chem. Soc. 137 (2015) 1305–1313.

[62] S. Suzuki, T. Suzuki, M. Kimura, Y. Takagi, K. Shinoda, K. Tohji, Y. Waseda, EXAFS characterization of ferric oxyhydroxides, Appl. Surf. Sci. 169 (2001) 109–112.

[63] B. Wang, X. Han, C. Guo, J. Jing, C. Yang, Y. Li, A. Han, D. Wang, J. Liu, Structure inheritance strategy from MOF to edge-enriched NiFe-LDH array for enhanced oxygen evolution reaction, Appl. Catal. B Environ. 298 (2021), 120580.

[64] X. Bo, R.K. Hocking, S. Zhou, Y. Li, X. Chen, J. Zhuang, Y. Du, C. Zhao, Capturing the active sites of multimetallic (oxy)hydroxides for the oxygen evolution reaction, Energy Environ. Sci. 13 (2020) 4225–4237.

[65] J. Huang, Y. Li, Y. Zhang, G. Rao, C. Wu, Y. Hu, X. Wang, R. Lu, Y. Li, J. Xiong, Identification of key reversible intermediates in self-reconstructed nickel-based hybrid electrocatalysts for oxygen Evolution, Angew. Chem. Int. Ed. 58 (2019) 17458–17464.

[66] M. Asnavandi, Y. Yin, Y. Li, C. Sun, C. Zhao, Promoting oxygen evolution reactions through introduction of oxygen vacancies to benchmark NiFe-OOH catalysts, ACS Energy Lett. 3 (2018) 1515–1520.

[67] J. Hwang, R.R. Rao, L. Giordano, Y. Katayama, Y. Yu, Y. Shao-Horn, Perovskites in catalysis and electrocatalysis, Science 358 (2017) 751–756.

[68] S. Li, Z. Li, R. Ma, C. Gao, L. Liu, L. Hu, J. Zhu, T. Sun, Y. Tang, D. Liu, J. Wang, A glass-ceramic with accelerated surface reconstruction toward the efficient oxygen evolution reaction, Angew. Chem. Int. Ed. 60 (2021) 3773–3780.

[69] H. Liao, T. Luo, P. Tan, K. Chen, L. Lu, Y. Liu, M. Liu, J. Pan, Unveiling role of sulfate ion in nickel-iron (oxy)hydroxide with enhanced oxygen-evolving performance, Adv. Funct. Mater. 31 (2021) 2102772.

[70] F. Bao, E. Kemppainen, I. Dorbandt, F. Xi, R. Bors, N. Maticiuc, R. Wenisch, R. Bagacki, C. Schary, U. Michalczik, P. Bogdanoff, I. Lauermann, R. van de Krol, R. Schlatmann, S. Calnan, Host, suppressor, and promoter—the roles of Ni and Fe on oxygen evolution reaction activity and stability of NiFe alloy thin films in alkaline media, ACS Catal. 11 (2021) 10537–10552.

[71] S. Klaus, Y. Cai, M.W. Louie, L. Trotochaud, A.T. Bell, Effects of Fe electrolyte impurities on $Ni(OH)_2/NiOOH$ structure and oxygen evolution activity, J. Phys. Chem. C 119 (2015) 7243–7254.

[72] D. Wu, X. Shen, X. Liu, T. Liu, Q. Luo, D. Liu, T. Ding, T. Chen, L. Wang, L. Cao, T. Yao, Insight into Fe activating one-dimensional α-$Ni(OH)_2$ nanobelts for efficient oxygen evolution reaction, J. Phys. Chem. C 125 (2021) 20301–20308.

[73] L. Trotochaud, S.L. Young, J.K. Ranney, S.W. Boettcher, Nickel-iron oxyhydroxide oxygen-evolution electrocatalysts: the role of intentional and incidental iron incorporation, J. Am. Chem. Soc. 136 (2014) 6744–6753.

[74] S. Lee, L. Bai, X. Hu, Deciphering iron-dependent activity in oxygen evolution catalyzed by nickel-iron layered double hydroxide, Angew. Chem. Int. Ed. 59 (2020) 8072–8077.

[75] D. Friebel, M.W. Louie, M. Bajdich, K.E. Sanwald, Y. Cai, A.M. Wise, M.-J. Cheng, D. Sokaras, T.-C. Weng, R. Alonso-Mori, R.C. Davis, J.R. Bargar, J.K. Nørskov, A. Nilsson, A.T. Bell, Identification of highly active Fe sites in (Ni,Fe)OOH for electrocatalytic water splitting, J. Am. Chem. Soc. 137 (2015) 1305–1313.

[76] Z. Xue, X. Li, Q. Liu, M. Cai, K. Liu, M. Liu, Z. Ke, X. Liu, G. Li, Interfacial electronic structure modulation of NiTe nanoarrays with NiS nanodots facilitates electrocatalytic oxygen evolution, Adv. Mater. 31 (2019) 1900430.

[77] Y. Wang, S. Tao, H. Lin, G. Wang, K. Zhao, R. Cai, K. Tao, C. Zhang, M. Sun, J. Hu, Atomically targeting NiFe LDH to create multivacancies for OER catalysis with a small organic anchor, Nano Energy 81 (2021), 105606.

[78] Y. Shi, W. Du, W. Zhou, C. Wang, S. Lu, S. Lu, B. Zhang, Unveiling the promotion of surface-adsorbed chalcogenate on the electrocatalytic oxygen evolution reaction, Angew. Chem. Int. Ed. 59 (2020) 22470–22474.